International Journal of Multiphase Flow 112 (2019) 155–169

Contents lists available at ScienceDirect

International Journal of Multiphase Flow

journal homepage: www.elsevier.com/locate/ijmulflow

Interaction of a cavitation bubble with a polymeric coating–scaling fluid and material dynamics

Georges L. Chahine*, Aswin Gnanaskandan, Amir Mansouri, Chao-Tsung Hsiao, Romain Content

Dynaflow, Inc., 10621-J Iron Bridge Road, Jessup, MD, USA

ARTICLE INFO

Article history:
Received 23 August 2018
Revised 28 November 2018
Accepted 17 December 2018
Available online 18 December 2018

ABSTRACT

Cavitation bubble dynamics and interaction with a polymeric coating material can be scaled in space and time using spark-generated bubbles near an appropriate soft material and can be simulated using fluid-structure interaction (FSI) modelling. In this paper, cavitation bubble dynamics in a high-pressure cavitating jet eroding a Polyurea layer on a rigid substrate is simulated using spark-generated bubbles operating at reduced pressures near an Agar layer of a properly selected concentration. Geometric scaling is based on the ratio of bubble maximum radii in the two configurations, and fluid dynamics scaling follows the Rayleigh scaling, i.e. lengths are normalized by the bubble maximum radius and times by the Rayleigh time. Scaling of the materials properties is achieved by equating the ratio of the materials mechanical properties (Young's and shear moduli) to the ratio of the local ambient pressures collapsing the bubble. Full FSI numerical simulations conducted at different scales with the two materials indicate the validity of the scaling.

1. Introduction

Compliant materials are increasingly used as coatings in naval applications and their resistance to cavitation is an important issue. Cavitation erosion results from the collapse of microbubbles forming shock waves and fast reentrant jets impacting on the material (Brennen, 1995; Hammitt, 1980; Kim et al., 2014). The response of the coatings involves large local accelerations of the material surface and strong feedback and modification of the bubble dynamics itself. However, the small spatial and fast temporal scales prevent adequate experimental measurements of these physical processes. Numerical simulations have investigated the dynamics of bubbles and materials' response but still require experimental validation (Chahine and Hsiao, 2015; Choi and Chahine, 2017; Duncan and Zhang, 1991; Hsiao et al., 2014; Madadi-Kandjani and Xiong, 2014). Cavitation is a dynamic phenomenon that occurs when the local pressure in the liquid drops below a critical pressure (often quoted to be the liquid vapor pressure for studies ignoring bubble surface tension), that causes the nuclei in the liquid to grow at a rapid rate (Borkent et al., 2009; Brennen, 1995; Chahine, 2004; Kim et al., 2014). When the pressure returns to a high value, bubble implosion occurs and generates high pressure pulses and shock waves. The collapse of these imploding bubbles have been shown (Chahine, 1982; Crum, 1979; Plesset and Chapman, 1971) to cause high-speed reentrant liquid jets, that upon impacting a nearby surface can cause severe damage and failure. Visualizing these reentrant jets experimentally and modeling and simulation of collapsing bubbles have been an active area of research (e.g. (Brujan et al., 2002; Chahine et al., 2002; Crum, 1979; Naude´and Ellis, 1961; Vogel et al., 1989; Zhang et al., 1993)).

Experimentally, spark generators have been used to produce large and relatively easy to control and visualize bubbles since the early works of Ellis (1965b). More recently, laser induced bubbles were introduced by Lauterborn and Bolle (1975) and have been extensively used since. Due to the extremely fast time scale and small length scales of cavitating bubbles, it is often impossible to visualize the bubble dynamics using high speed photography. It is therefore desirable to slow down the dynamics and also increase the length scales to facilitate visualization, while maintaining the same underlying physics in both the liquid and in the material. In this study, we therefore introduce a scaling approach that makes observation and measurement of the bubble dynamics and the material structural dynamics possible. In lab-scale visualizations, the bubble dynamics is slowed down and the length scales are increased using classical spark-generated bubbles in a vacuum tank (Chahine et al., 1995; Goh et al., 2017; Jayaprakash et al., 2012; Kling and Hammitt, 1972; Ma et al., 2018b). This, however, is not sufficient to properly observe the FSI, since the material of the

* Corresponding author.
E-mail address: glchahine@dynaflow-inc.com (G.L. Chahine).

https://doi.org/10.1016/j.ijmultiphaseflow.2018.12.014
0301-9322/

coating exposed to the full-scale cavitation (e.g. Polyurea in this study) also has to be replaced in the scaled condition by a material with mechanical properties scaled down from those of Polyurea to match the level of pressure loadings from the spark-generated bubbles. Thus, in the scaling method presented in this paper, fast collapsing microscopic cavitation bubbles on Polyurea are replaced with centimeter sized slower spark-generated bubbles interacting with an Agar layer at a specific concentration. This enables one to validate the numerical FSI simulation procedure, to visualize bubble and material behavior, and to predict the behavior of microscopic bubbles on Polyurea.

The dynamics of bubbles and bubbly flows and their interaction with nearby bodies, in the absence of structural deformation, have been studied effectively using boundary element based methods (Kinnas and Fine, 1994; Wang and Khoo, 2004; Zhang et al., 1993) Eulerian homogenous mixture models (Gnanaskandan and Mahesh 2015; Kinzel et al., 2009; Singhal et al., 2002) and Euler-Lagrange based methods (Fuster and Colonius, 2011; Ma et al., 2015, 2018a). However, in practical applications, the structural response, can significantly affect the bubble dynamics, which controls structural loading, stresses, erosion and damage. Significant effects due to the structural response on the bubble dynamics are observed including modification of the bubble period, modification of the reentrant jet formation, and pressure generated on the deformable surface (Chahine and Hsiao, 2015; Chahine and Kalumuck, 1997; Duncan and Zhang, 1991). These results indicate that structural characteristics can significantly affect erosion and damage to a structure by nearby cavitation or explosion bubbles. Reliable prediction of loads on materials and bodies requires fully coupled fluid-structure modeling. Due to the complexity of the problem at hand only specialized numerical methods presently offer hope for efficient and accurate solution to the problem. In this study we utilize a fully coupled fluid structure solver (Chahine et al., 2015; Hsiao et al., 2014; Luton et al., 2004; Wardlaw and Luton, 2003)

This paper is organized as follows. We first discuss the scaling approach and then the experimental and numerical methods used. We then show that the numerical simulations recover the experimental spark-generated bubble results. With this established, we show numerically, using normalized plots, that the results of the microscopic high-pressure cavitation bubbles collapsing on Polyurea are the same as those obtained in the spark tank conditions on an Agar layer selected to have the proper material properties and thickness. We then discuss the physical parameters, which are not conserved between the scales and which interfere with having a perfect correspondence between scaled conditions.

2. Basis of the scaling approach

To scale properly the bubble dynamics, the following scaling has been classically used (Brennen, 1995). The bubble radius - or any selected length on the bubble shape - is normalized with the bubble maximum radius R_{max}, and time is normalized with the Rayleigh time,

$$T_{Rayleigh} = R_{\max}\sqrt{\rho/P_{amb}}, \tag{1}$$

where ρ is the liquid density and P_{amb} is the local liquid ambient pressure in the vicinity of the bubble. With this normalization, non-dimensional bubble size versus non-dimensional time curves fall on top of each other for all conditions (except for large variations in the internal gas pressures, viscosity or surface tension of the bubbles). This means that one can deduce the dynamics for any condition once only one reference condition is known. A spark-generated test will then provide scaled results for microscopic as well as for meter-sized bubbles (ignoring terms that have been shown to have, in general, secondary effects such as viscosity, gas pressure, and surface tension). Near a rigid boundary, at a distance X from the bubble center, the same scaling applies, provided that the normalized distance, $\bar{X} = X/R_{\max}$, is conserved.

Near a deformable coating layer, this scaling is still valid, provided however, that the thickness of the coating is also scaled with R_{max} and that the ratio between the characteristic impulsive pressure generated by the bubble collapse at the boundary and the ratios of the parameters characterizing the material resistance to the load are the same. The relevant parameters here are the material Young modulus, E, the shear modulus, G, and the bulk modulus, K. Material characteristic times τ are expressed below in terms of material density ρ_m, moduli, and maximum bubble radius.

$$\begin{aligned}\tau_E &= R_{\max}\sqrt{\rho_m/E},\\ \tau_K &= R_{\max}\sqrt{\rho_m/K},\\ \tau_G &= R_{\max}\sqrt{\rho_m/G},\end{aligned} \tag{2}$$

The ratio between these times and the Rayleigh time needs to be conserved, Correct material response with increased time scales is ensured by maintaining the following ratios

$$\frac{\rho_m}{\rho}\frac{P_{amb}}{E}, \qquad \frac{\rho_m}{\rho}\frac{P_{amb}}{K}, \qquad \frac{\rho_m}{\rho}\frac{P_{amb}}{G}. \tag{3}$$

In this study, we examine Polyurea, which is of interest because of its good performance against shock waves from explosions. Its resistance to cavitation erosion has been investigated in (Choi and Chahine, 2017; Marlin and Chahine, 2018) and its relevant material properties are listed in Table 1 (Amirkhizi et al., 2006).

For material scaling purposes, we performed large-scale spark tests in the laboratory using various concentrations of Agar, which has been used in studies of biological effects of cavitation (Movahed et al., 2016). Agar is a viscoelastic material like Polyurea, and has shear and Young's moduli, which are much smaller than those of Polyurea (Nayar et al., 2012). As shown in Table 1, with 5% Agar powder mixed with water, the Young and shear moduli (which are related through the Poisson ratio, $E = 2G(1+\nu); \quad \nu \simeq 0.5$) are about 30 times smaller than the Polyurea values, while the bulk moduli are about the same. However, the numerical simulations presented below confirm that K is less relevant for the present problem (see the Section "Effects of Materials Properties"), as it relates to acoustic wave propagation time scales much smaller than those involved during the dynamics of the bubble of interest here.

Table 1 also shows the properties of a 0.5% Agar mixture. The Young's and shear moduli are in the same range, i.e. ~500 times less than for Polyurea, while the ratio of the bulk moduli is about 1. Changing the concentration of Agar changes the ratios discussed above and thus results in simulating smaller or larger impact loading ranges. The elastic properties of Agar and Polyurea have been considered to be constant in this study. However, in reality, these properties are frequency dependent (Ando, 2015; Jamburidze et al., 2017; Nayar et al., 2012). The effect of change in elastic properties with frequency cannot be accounted for in a simple viscoelastic model like the one considered in this study, but should be considered in future studies.

Table 2 compares the local ambient pressures, P_{amb}, between spark-generated bubble test conditions for Agar and a typical pressure in the stagnation region of a cavitating jet impacting on a Polyurea coated plate since cavitating jets are commonly used to test materials for their resistance to cavitation erosion (Chahine et al., 2014). Note that the impulsive pressures from cavitation bubble collapse are proportional to the local ambient pressure driving the bubble collapse, P_{amb}. Since the ratio of the erosion resistance characteristics (E, G) of the two materials (Polyurea, Agar) is about 30 for 5% Agar, a spark test conducted at a tank pressure of ~0.1 MPa, should scale properly cavitating jet bubble behavior on Polyurea in a ~3 MPa (~450 psi) jet, which is below the threshold for significant damage. However, if 0.5% Agar

Table 1
Properties of materials.

Material	PU	Agar 5%	Agar 0.5%	Ratio PU/Ag5%	Ratio PU/Ag0.5%
Young Modulus, E (MPa)	67	2.2	0.134	30	500
Shear Modulus, G (MPa)	22.2	0.73	0.045	30	493
Bulk Modulus, K (MPa)	3000	2370	2370	1.3	1.3
Density (Kg/m^3)	1100	999	992	1.10	1.11

Table 2
Liquid and bubble conditions.

Fluid conditions	PU	Agar 5%	Ratio PU/Ag 5%	PU	Agar 0.5%	Ratio PU/Ag 0.5%
P_{amb} (MPa)	3	0.10	30	7	0.014	500
R_{max} (mm)	0.1	10	0.01	0.1	20	0.005

(where the material resistance ratio increases to ~500) is used at a spark test tank ambient pressure of 0.014 MPa (2 psi), a ~7 MPa (~1000 psi) cavitating jet interaction with Polyurea can be simulated. A whole range of selections is possible to simulate various levels of cavitation erosion on Polyurea by selecting the ambient pressure in the spark tank and the percentage of Agar in the mixture.

3. Experimental setup

Spark bubbles have been used for many decades since the early work of Ellis (1965) to simulate cavitation and underwater explosion bubbles. In the present study, the bubbles are generated by very fast underwater discharge of a high-voltage charge stored in capacitors between two coaxial electrodes. The electrical energy is converted into small volume plasma which has temperatures as high as 20,000 K, and pressures as high as 10^9 Pascals (Kling, 1970). Because of the high pressure, the liquid near the plasma interface is initially compressed. The pressure in the gas sphere then quickly falls but is well above that of the surrounding liquid. From this point on, incompressible hydrodynamic effects dominate. The pressurized gas expands into a relatively large bubble, which subsequently collapses and re-expands. The phenomena preceding the incompressible hydrodynamic phase occur quickly and are accompanied by light generation that prevents accurate determination of the initial bubble radius using conventional high-speed photography. In the present study, the sparks are generated between two coaxial Stainless Steel 316 electrodes. The outer cylindrical electrode has a 2.1 mm outer diameter, while the diameter of the inner one is 0.38 mm. The two electrodes are separated by a 0.25 mm layer of Polytetrafluoroethylene (PTFE). The dynamics of the spark-generated bubbles away from boundaries have been shown to follow the Rayleigh–Plesset equation (Chahine et al., 1995). The energy supplied to the spark is controlled by the voltage applied to the capacitor of the spark generator and by the size of the capacitor. In cases where the bubble is significantly far from boundaries, it retains a spherical shape up to the time of maximum volume and a sphere's radius could be easily measured. In cases where the bubble is distorted by the presence of boundaries, an equivalent radius can be derived. Here, it is obtained by assuming the bubble to be axisymmetric and calculating the volume as that of a solid of revolution of the observed outline around an axis of symmetry.

The experimental setup used in this study is illustrated in Fig. 1. It consisted of: (a) a 60 cm × 60 cm × 60 cm Plexiglas tank with 5-cm thick walls needed to enable one to reduce the ambient pressure well below the atmospheric pressure, (b) a spark generator system, which discharges the energy stored in the capacitor across the gap between coaxial electrodes, (c) a vacuum pump, (d) a high-speed camera and two LED lights, (e) a Plexiglas structure inside the tank where the Agar plate and electrode are mounted, and (f) a computer system to control the spark energy and synchronize with the high-speed imaging. The agar plates were soaked in the water for one day before running the test described below.

To generate larger bubbles and enhance the observation of the bubble-Agar interaction, the tests were performed under low ambient pressure using the vacuum pump. For post-test analysis, the ambient pressure was calculated based on the measured pressure above the free surface in the tank plus the hydrostatic head at the location of the electrodes. The vapor pressure was deduced from the ambient water temperature. An IDT Y-series model high-speed camera was used to record the bubble evolution at framing rates between 3000 and 100,000 frames per second. A small exposure time of each frame, 90 μs was used to capture the bubble shape and formation of reentrant jet sharply. Two LED lights illuminated the front side of the test tank.

As illustrated in Fig. 1, in order to improve the visualization and obtain larger bubbles, the electrodes were located flush with the visualization Plexiglas wall, i.e. the wall through which the high-speed movies were recorded. A half-sphere bubble was therefore generated, and because of the principle of images in potential flow, reproduces the behavior of a full bubble after including the image. The effects of the presence of the plane of symmetry wall (surface tension and viscosity, which are reflected in the pictures as a very small curved edge of the interface gas-water-Plexiglas) are minimal and have negligible effects on the bubble dynamics and on the visualization. The transparent plane of symmetry wall allows very good recording of the bubble deformation, including good visualization of the reentrant jet (see for example Fig. 2 for a bubble in the gravity field).

In addition to visualizing clearly the inside of the bubble, the transparent plane of symmetry allows one to visualize a cut through the Agar coating layer in the plane of symmetry. We took advantage of this view to evaluate the deformations and strains inside the Agar coating. In order to do so, dark dot particles were inserted as markers and were distributed regularly in the coating thickness and along the axisymmetric bubble/coating configuration radial direction from the axis of symmetry (see Fig. 3). Another plate with uniform holes was utilized to insert the markers in the agar plate with uniform distribution. This enabled us to follow the particle motion in time using the high-speed photography and then to deduce deformations, strains, and strain rates.

3.1. Characterization of spark generated bubbles

The spark generator system used in this work has been extensively used to simulate bubble dynamics and underwater explosion bubbles. The size and period of a generated bubble are directly controlled by the voltage, V, used to charge the capacitor, C, and by the selected pressure inside the spark tank, P_{amb}. The electric energy delivered is $E_e = 0.5CV^2$. However, most of this energy is lost

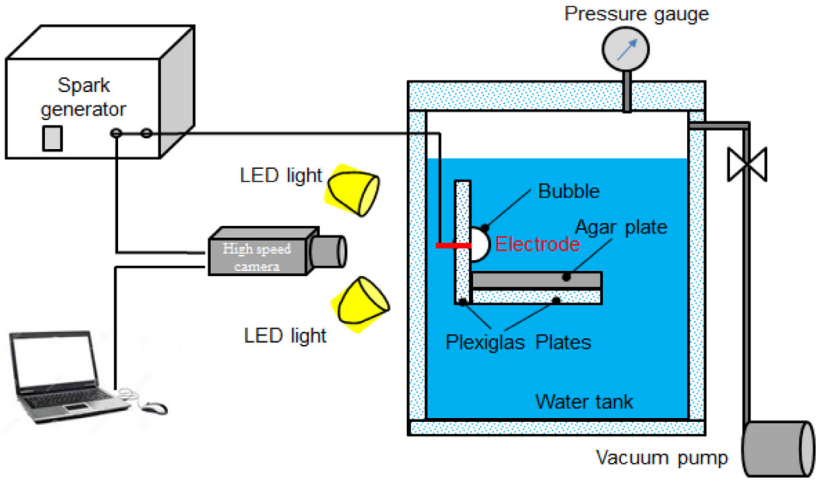

Fig. 1. Experimental setup to produce and visualize spark-generated bubbles and their interaction with nearby boundary such as an Agar layer. In this setup, using the principle of images, only half of a bubble is generated to improve visualization. A full bubble over the middle of the plate would produce the same results.

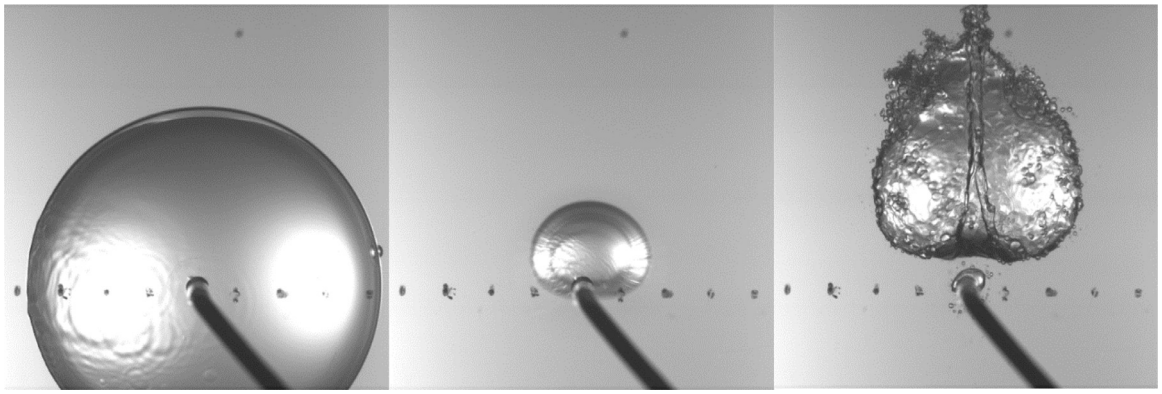

Fig. 2. Spark-generated bubble collapse in gravity showing clearly an upward moving reentrant jet. Note that the electrodes are flush with the symmetry wall and do not intrude in the flow. The electrode wires seen as a black thick line are outside of the tank.

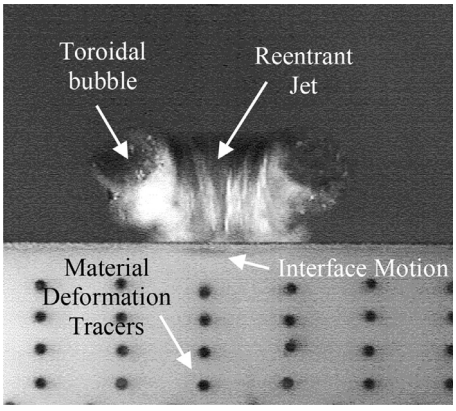

Fig. 3. Picture from a high-speed movie of bubble collapse near a deformable coating, showing the toroidal bubble resulting from the reentrant jet crossing the opposite bubble wall. The motion of the inserted dots inside the coating provides the strain rates in the material.

in the sparking and shock wave formation and only about 5% of E_e, $E \simeq 0.05E_e$, is actually transferred into the bubble. Fig. 4 illustrates calibration curves for a bubble generated away from boundaries. It shows the maximum bubble radius achieved versus the electric voltage, V, for a set of values of the ambient pressure, all with a capacitor of 1 μF. For a given voltage, the bubble size increases when the ambient pressure is reduced. Similarly, at a given ambient pressure, the bubble size increases with the voltage.

It is well known for underwater explosion that the maximum bubble radius generated at a given depth, or P_{amb}, is directly proportional to one third power of the ratio of the explosion energy and the depth (Cole, 1965; Snay and Christian, 1952),

$$R_{\max} = J_1 \left(\frac{E}{P_{amb}} \right)^{1/3}, \tag{4}$$

where J_1 is an explosive type dependent constant. We have established that this relationship applies also for the spark bubbles, as shown in Fig. 5. If we plot R_{max} as a function of the energy in the spark bubble divided by the ambient pressure, E/P_{amb}, all data points from Fig. 4 collapse on a single curve, which has a 1/3 power. Note that in (4) R_{max} is based on the volume of a full sphere. In the cases considered in the present experiments, the spark is generated at the wall, in the plane of symmetry, and the gas volume is deposited in a half sphere. The resulting radius is therefore $2^{1/3}$ larger. In the figure the corresponding radii were divided by $2^{1/3}$ to account for this fact.

4. FSI numerical simulations model

In parallel to the experimental work, the interaction of a growing and collapsing bubble with a nearby layer of a polymeric material was modeled using coupled fluid and structure codes. The fluid was modeled using a multi-component fully compressible

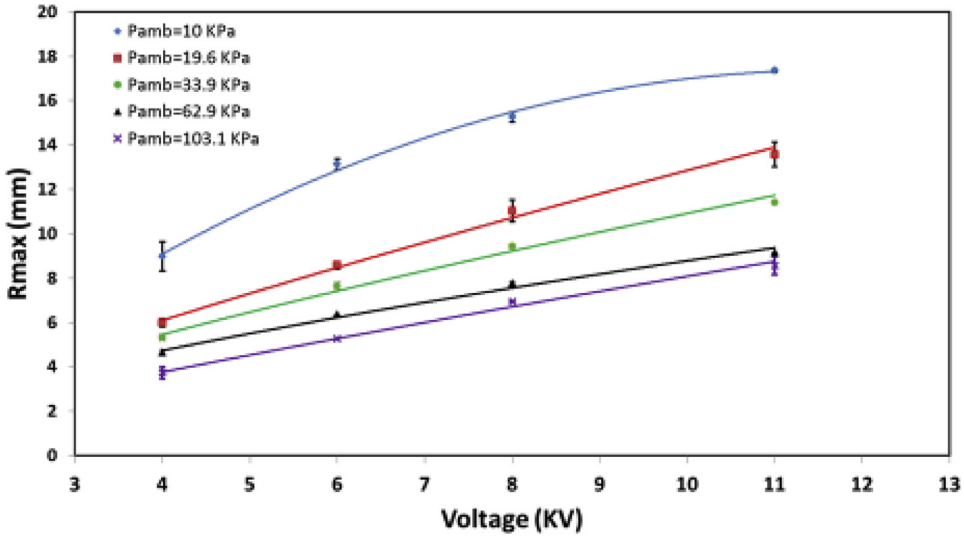

Fig. 4. Bubble maximum radius, R_{max}, versus voltage in the spark generating system for different ambient pressure in the test tank.

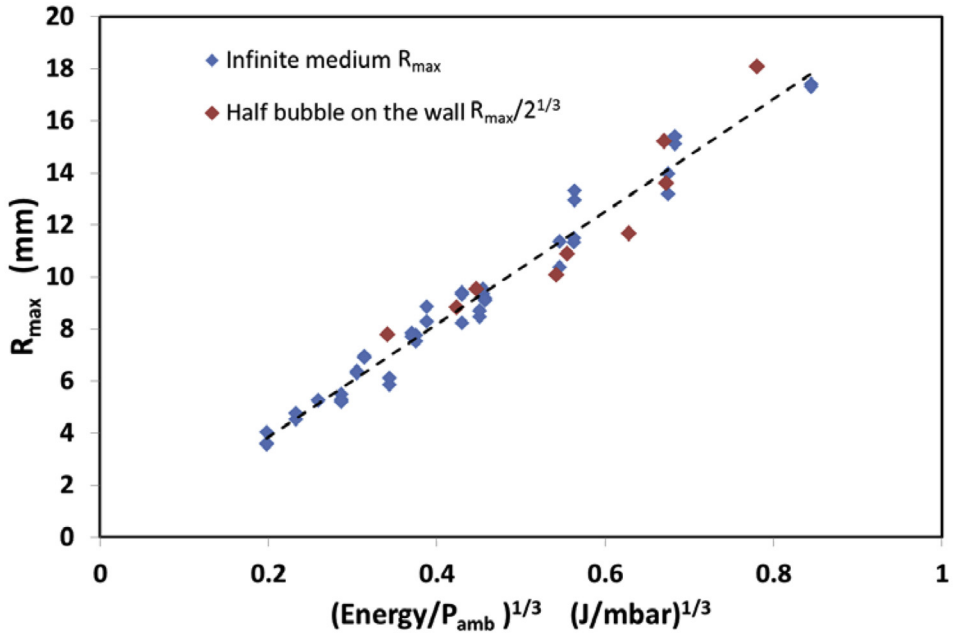

Fig. 5. Maximum bubble radius versus the energy, E_e, in the spark divided by the ambient pressure raised to the one third power.

flow solver, which is able to capture shock waves and handle liquid / gas /material interfaces. This was coupled with a finite element method structural code. Both codes are components of the US Navy code DYSMAS. The numerical modeling includes description of the bubble dynamics near the deformable coating and fluid-structure interaction (Chahine, 2014; Chahine and Hsiao, 2015; Choi and Chahine, 2017). The resulting deformations in the material were computed and the predictions were compared with the spark-generated bubbles. Additional computations were conducted to demonstrate the validity of the scaling approach described above.

4.1. Compressible flow solver

The multi-material compressible Euler equation method used in this study can capture nonlinear acoustic and shock wave propagation in multi-material media by solving the following continuity, momentum, and energy equations in a fixed Cartesian grid (Kapahi et al., 2015; Wardlaw and Luton, 2003):

$$\begin{aligned}
&\frac{\partial \rho_m}{\partial t} + \nabla \cdot (\rho_m \mathbf{u}) = 0,\\
&\frac{\partial \rho_m \mathbf{u}}{\partial t} + \nabla \cdot (\rho_m \mathbf{u}\mathbf{u}) = 0,\\
&\frac{\partial \rho_m E_m}{\partial t} + \nabla \cdot ((\rho_m E_m + p_m)\mathbf{u})) = 0,
\end{aligned} \tag{5}$$

where ρ_m is the medium density, p_m is the pressure, $E_m = e_m + 0.5\mathbf{u}^2$ is the total energy, e_m is the internal energy, and $\mathbf{u}$ is the velocity vector. Here, m indicates mixture of liquid, l, and gas, g, quantities, defined as:

$$\begin{aligned}
\rho_m &= \rho_l \alpha_l + \rho_g \alpha_g,\\
P_m &= \frac{\alpha_l \rho_g c_g^2 P_l + \alpha_g \rho_l c_l^2 P_g}{\alpha_l \rho_g c_g^2 + \alpha_g \rho_l c_l^2},
\end{aligned}$$

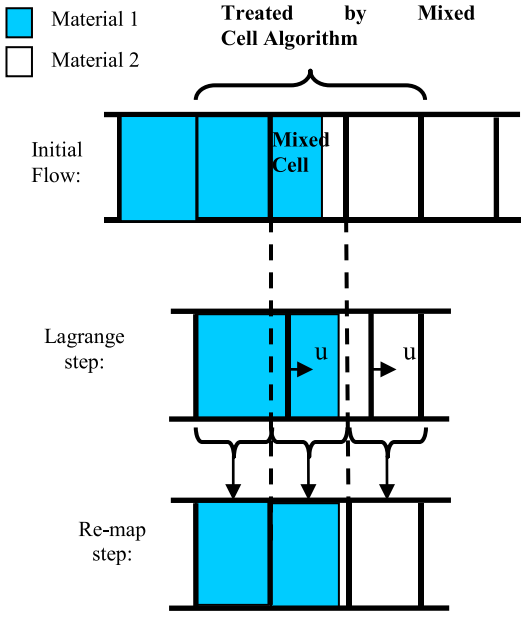

Fig. 6. Illustration of the mixed cell algorithm procedure.

$$e_m = \frac{1}{\rho_m}[\rho_l \alpha_l e_l + \rho_g \alpha_g e_g], \tag{6}$$

where α_i is the volume fraction of component i and c_i is the corresponding sound speed. The liquid-gas mixture density, pressure, and energy are obtained from their components' corresponding values or governing equations. Here, a γ-law (with $\gamma = 1.4$) is used for air:

$$p_g = (\gamma - 1)\rho_g e_g, \tag{7}$$

and the Tillotson equation is used for water (Zel'dovich and Raizer, 2012):

$$p_l = p_{l,0} + \omega \rho_l (e_l - e_{l,0}) + A\mu + B\mu^2 + C\mu^3,$$
$$\mu = \frac{\rho_l}{\rho_{l,0}} - 1, \tag{8}$$

where ω, A, B, C are constants associated with water and $p_{l,0}$, $e_{l,0}$ and $\rho_{l,0}$ are the reference pressure, specific internal energy, and density, respectively. The following default values for water were used in the computations:

$$\rho_{l,0} = 1000\ kg/m^3, \omega = 0.28, A = 2.20 \times 10^9\ Pa,$$
$$B = 9.54 \times 10^9\ Pa, \quad C = 1.48 \times 10^{10}\ Pa,$$
$$e_{l,0} = 3.54 \times 10^5\ m^2/s^2, \quad p_{l,0} = 1.0 \times 10^5\ Pa. \tag{9}$$

The standard MUSCL scheme is augmented by the mixed cell approach to handle material interfaces. For multiple materials, the single fluid algorithm advances the solution first by using temporal average properties. The cells containing the material interfaces and their immediate neighbors known as "mixed cells" are revisited and re-solved using a fully conservative "Lagrange plus remap" step. In the Lagrange step, cell edges that are adjacent to mixed cells are moved at local fluid velocities approximated by the previously computed Riemann slip velocity (corrector step), while edges with pure cells on both sides are held fixed (Kapahi et al., 2015). Thus, mixed cells are treated from the Lagrange point of view, while adjacent pure cells have one edge that moves at the local fluid velocity and a stationary one. During the re-map step, the convected flow is mapped back to the original grid. The process is illustrated in Fig. 6.

4.2. Structure dynamics solver

To model the dynamics of the material, the finite element model Dyna-N(2D) is used (Whirley and Engelmann, 1993). Since the problem considered here is axisymmetric, we used this axisymmetric version of Dyna-N to speed up the computations. Dyna-N(2D) is a non-linear explicit structure dynamics code developed by the Lawrence Livermore National Laboratory. Here it computes the material deformation when the loading is provided by the fluid solution. Dyna-N(2D)uses a lumped mass formulation for efficiency. This produces a diagonal mass matrix **M,** to express the momentum equation as:

$$\mathbf{M}\frac{d^2\mathbf{x}}{dt^2} = \mathbf{F}_{\text{ext}} - \mathbf{F}_{\text{int}}, \tag{10}$$

where $\mathbf{F}_{\text{ext}}$ represents the applied external forces, and $\mathbf{F}_{\text{int}}$ the internal forces. The acceleration,$\mathbf{a} = d^2\mathbf{x}/dt^2$ for each element, is obtained through an explicit temporal central difference method. Additional details on the general formulation can be found in Whirley and Engelmann (1993).

4.3. Material models

In the present study, Polyurea and Agar at concentrations of 0.5% and 5% are considered. Both Polyurea and Agar are modeled as viscoelastic materials. In the standard Dyna-N model (Key, 1974), the deviatoric stresses of a viscoelastic material are found from

$$s_{ij}(t) = 2\int_0^t G(t-\tau)D'_{ij}d\tau, \tag{11}$$

where D'_{ij} is the deviatoric strain rate and the function $G(t)$ describes the shear relaxation behavior over time

$$G(t) = G_\infty + (G_o - G_\infty)e^{-\beta t}. \tag{12}$$

The volumetric response is elastic, so the pressure p is computed from the current volumetric strain using

$$p = -K\varepsilon_{Vol}, \tag{13}$$

where K is the elastic bulk modulus and ε_{Vol} is the volumetric strain. In the above equations, G_∞ is the long-time shear modulus, G_o is the short-time shear modulus, and β is a decay constant. While the elastic constants K and G_o used in the simulations are described in Table 1, the decay constant used in the simulation is 4×10^{-5} and the ratio G_0/G_∞ is 2.0.

4.4. Coupling fluid and structural solvers

The coupling between liquid and structure solutions is executed at each time step of the simulation according to the following coupling procedure:

- At the end of a given fluid time step, the fluid code provides the computed pressure loading at the center of the fluid-material interface to the structure dynamics code.
- The structure code computes material stresses and strains and provides back to the fluid code the deformations and velocities of the fluid-structure interface in response to this loading.
- The fluid code then solves the flow field at the new time step and deduces the pressures at the interface using the positions and velocities of the surface as boundary conditions.
- The coupling cycle continues until the end of the simulation.

5. Results and discussion

5.1. Initialization of bubble computations

Initialization of the bubble dynamics in the compressible code is not trivial and has to be done properly (Lauterborn et al., 2018).

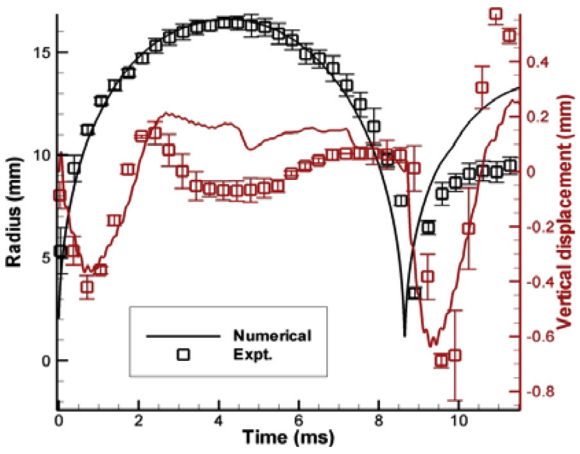

Fig. 7. Comparison of bubble equivalent radius and vertical displacement of the Agar layer interface between experiments and simulations: $\bar{X} \sim 1.52$, $P_{amb} = 0.014$ MPa, $R_{max} \sim 17$ mm; thickness of the 5% Agar layer = 19 mm. The equivalent radius is computed from the surface of the bubble in the images and assuming the bubble shape axisymmetric. Uncertainty increases following reentrant jet impact.

Here, we have considered two options. One was to simulate the spark as a micro-explosion and use an approach validated for regular explosives to initiate the bubble (Chahine et al., 1995; Jayaprakash et al., 2012). This requires a fraction of a microgram of TNT. The approach works well but additional work is needed to validate it for cavitation bubbles. Instead, we selected the second method, where the initial phase of the spark generation is ignored, and the bubble dynamics is initiated using a highly compressed gas (here air) in an initially small spherical bubble. This is a common approach in the bubble dynamics literature starting with the Rayleigh–Plesset equation (Rayleigh, 1917, Plesset, 1964) and including actually modeling underwater explosion and cavitation bubbles with potential flow codes (Choi and Chahine, 2003; Hsiao and Chahine, 2015). The initial conditions inside the bubble involve an unknown very high pressure, $P_{g0,}$ and an initial radius R_0. Further, the compressible code requires the initial energy or the initial density of the gas inside the bubble, which obviously has to be consistent with P_{g0} and R_0. Since these initial conditions will dictate the evolution of the bubble, we have established a procedure to compute these initial conditions correctly in order to ensure a proper bubble evolution. The maximum radius that the bubble expands to, R_{max}, is known from the experiments along with ambient pressure P_{amb}. We first assume an initial radius R_0 and compute P_{g0} using the following relation derived from the Rayleigh–Plesset equations (Krieger and Chahine, 2003):

$$P_{g0} = (P_{amb} - P_v)\frac{(1-k)\left(1-\varepsilon^{-3}\right)}{1-\varepsilon^{3k-3}}, \qquad \varepsilon = \frac{R_0}{R_{max}}, \tag{14}$$

where P_v is the liquid vapor pressure. The gas is assumed to be ideal and to follow a gas compression law with compression coefficient k,

$$P_{g,ref} {R_{ref}}^{3k} = P_{g0} {R_0}^{3k}. \tag{15}$$

Here, we use $k = 1.4$ and compute the radius corresponding to a reference condition. Knowing the isentropic relation between density and volume at reference conditions and initial conditions, the initial density inside the bubble is then computed. The P_{g0} computed from the above equation does not account for compressible effects and does not account for shock energy losses during the initial bubble expansion. Hence, the value of P_{g0} is changed iteratively in the solution of the fully compressible code in order to obtain the desired R_{max} starting with the isentropic P_{g0} as an initial guess.

5.2. Validation of numerical FSI model with experiments

The FSI model described above is first validated by comparison against spark experiments. We present below results obtained at two different non-dimensional standoff distances $\bar{X} = 1.52$ and $\bar{X} = 1.05$. The spark generated bubble tests were conducted at low ambient pressure, $P_{amb} \simeq 0.014$MPa, using a 19 mm thick layer of 5% concentration of Agar over a 12.7 mm thick Plexiglas substrate (assumed fully rigid). The spark generated bubbles under these conditions were of the order of 20 mm radius and were easy to visualize with a high-speed camera operating at framing rates of the order of 10,000 fps. Fig. 7 shows in black symbols the bubble equivalent radius and in red symbol the displacement of the center of the

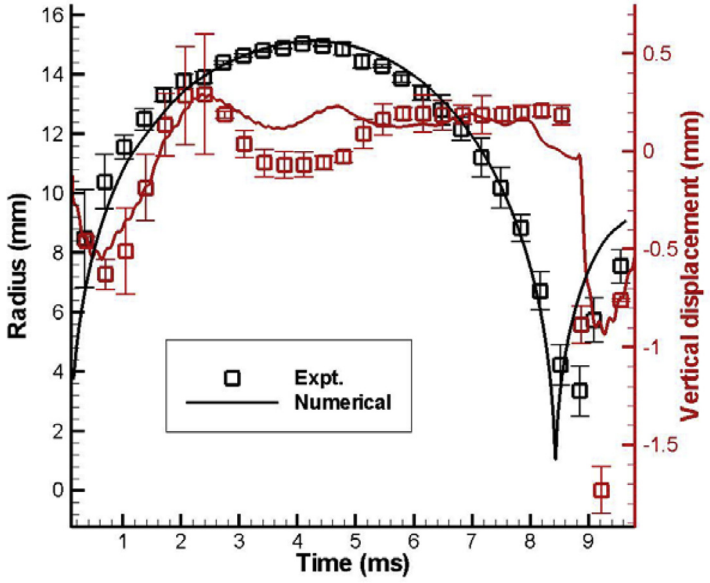

Fig. 8. Comparison between experiment and simulations of the bubble equivalent radius and the vertical displacement of the center of the Agar layer interface with water. $\bar{X} = 1.05$. Spark test conditions: $P_{amb} = 0.014$ MPa, $R_{max} \sim 16$ mm; thickness of Agar layer = 19 mm.

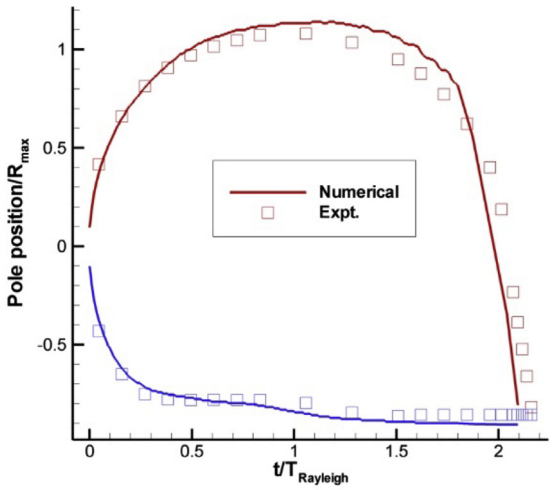

Fig. 9. Comparison of north and south pole normalized positions versus normalized time on the bubble between experiment and simulation for $\bar{X} = 1.05$. $\tau_{Rayleigh} = 4.009\ ms$.

Agar water interface. Also shown in the figure are the comparative results from the FSI simulations which used the material properties for 5% Agar shown in Table 1. A very good agreement for the bubble equivalent radius and an overall good agreement of the vertical displacement of the center of the square Agar plate-water interface can be seen. Following initiation of the bubble growth, a high-pressure wave is emitted from the spark center. The material responds by moving away from the bubble center but with a delayed response. A maximum negative displacement is achieved after a response time, τ_m, which depends on the Young modulus and the thickness of the Agar layer (Kulik, 2007). A second large negative displacement is also produced after the collapse of the bubble and the impact of the reentrant jet at the material-water interface. The loading due to the re-entrant jet impingement is one of the main causes of material failure and cavitation erosion (Chahine, 2014). Very good comparison is obtained for these two compression events at $t = 1$ ms and 9.5 ms.

During the bubble growth and close to R_{max}, we can see the largest discrepancy between the test and the simulation. The spark test results for the Agar motion are more significant during this stage than is computed numerically. So far, we could not identify clearly the reason for this discrepancy, which could be related to a combination of experimental uncertainties, uncertainties in the material properties used, and the simplicity of the viscoelastic structural model. We will investigate this further in the future.

Fig. 8 considers a closer standoff distance, $\bar{X} = 1.05$, between the bubble and the Agar layer than that shown in Fig. 7. The figure compares the bubble equivalent radius and the displacement of the Agar-water interface center. Here too, as expected, an excellent agreement is obtained for the radius evolution, the maximum radius and the bubble period. The first trough in the displacement of the Agar layer at 1 ms is predicted well. However, while the overall shape of the displacement function during the reentrant jet dynamics is captured quite well, the actual maximum dip in the displacement curve at 9.5 ms is under-predicted. There is also some discrepancy in the maximum bubble volume region. The reason for these discrepancies can be attributed to either the lack of resolution while capturing the re-entrant jet or are due to the validity of the material model at large displacements. Further investigations are being carried out to resolve this issue.

While Figs. 7 and 8 have shown comparisons between simulations and experiments of the bubble equivalent spherical radius based on the projected area of the bubble, a more precise quantitative comparison of the bubble deviation from the spherical shape can be obtained by tracking the location of the north and south pole of the bubble during the growth and collapse phase. This is performed in Fig. 9, which shows the locations of the bubble poles (top and bottom points on the axis) for both the experiment and the simulation. This way of plotting clearly shows that the bottom of the bubble (blue lines and symbols) is limited in its motion due to the presence of the wall. During the collapse phase, this part of the bubble stays practically in about the same location, while the opposite side (red lines and symbols) moves very fast toward the wall since it is tracking the tip of the reentrant jet as it penetrates rapidly the bubble. Comparison between experiments (symbols) and simulation (solid lines) appears to be very good with the pole locations predicted satisfactorily by the simulation both during the bubble growth and collapse phase. There are some discrepancies during the collapse phase due to a combination of time and size errors of a couple of percent each. The corresponding bubble shape evolution and reentrant jet advance towards the coating during the bubble collapse can be clearly seen in Fig. 10.

Fig. 11 shows a similar case as in Fig. 10 but for a closer normalized standoff, $\bar{X} \sim 1$. This is shown because it captured quite clearly the various important stages of bubble growth and collapse. The figure also shows clearly the reentrant jet development ($t \sim 9.7$ ms) and formation of a well outlined cavitating vortex ring (here half of a torus) with a trail of microbubbles highlighting the jet impact on the wall ($t \sim 10$ ms), then the collapse of the ring at the wall ($t \sim 10.3$ ms). Here again a relatively large indentation is formed at the wall.

A more complete comparison of the bubble shapes between the experiment taken in the window plane of symmetry and the simulation at four non-dimensional times,

$$\tilde{t} = t/T_{Rayleigh}, \tag{16}$$

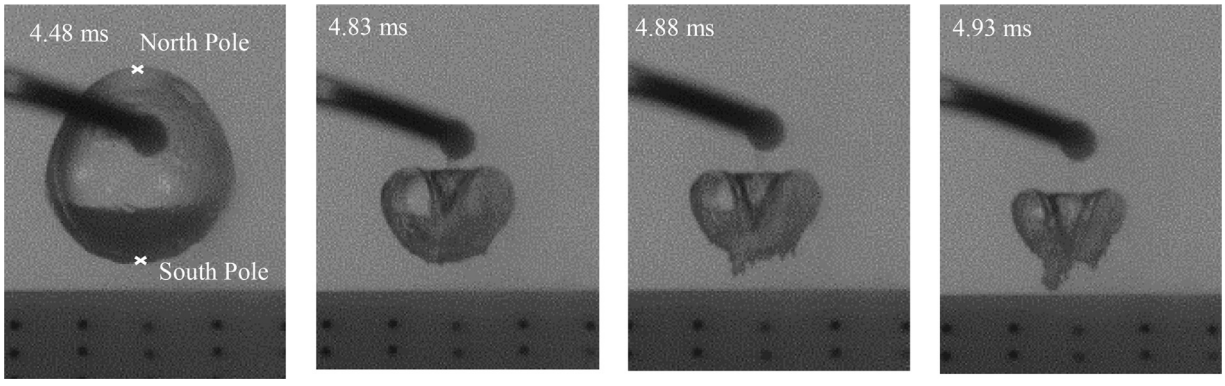

Fig. 10. Time sequence of a spark-generated bubble near a 5% Agar plate in a vacuum chamber. $P_{amb} \simeq 0.026$ MPa, $\bar{X} \simeq 1.05$, $R_{max} \sim 11$ mm; thickness of Agar layer = 19 mm.

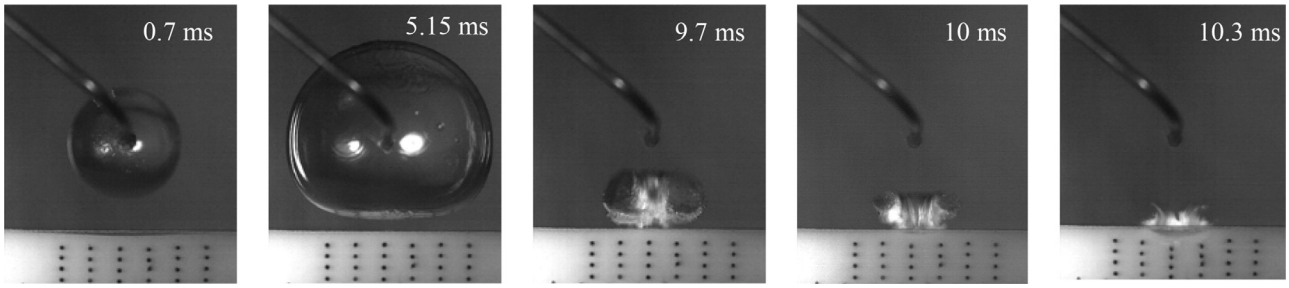

Fig. 11. Time sequence of a spark-generated bubble near a 5% Agar plate in a vacuum chamber. $P_{amb} \simeq 0.014$ MPa, $\bar{X} \simeq 1$.

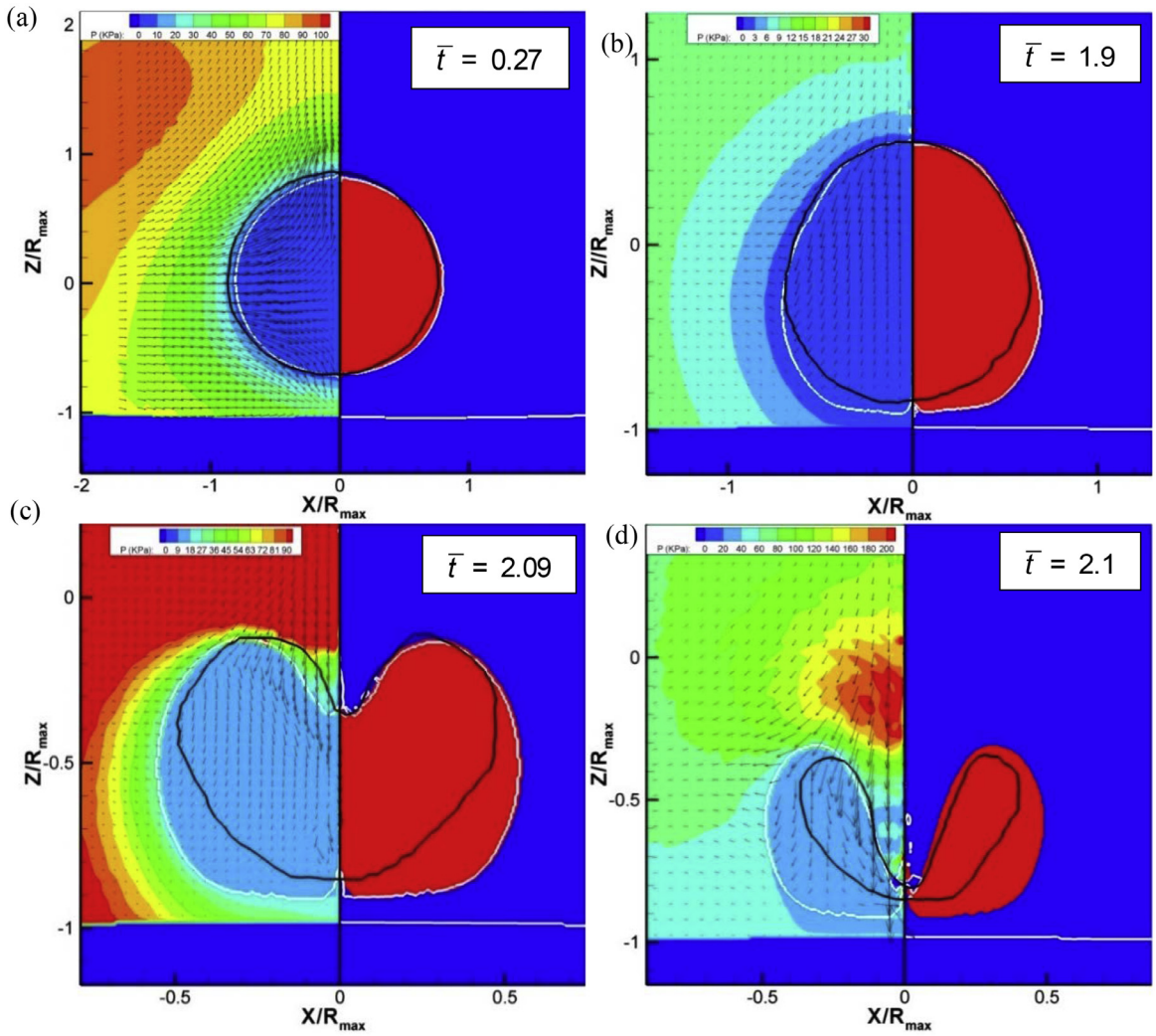

Fig. 12. Comparison of bubble shapes from experiment and simulations for $\bar{X} = 1.05$. The black lines are experimental bubbles shapes and white lines are simulation bubble shapes. The vector plot on the left frame shows the local instantaneous velocity while the contour color in the left frame represents pressure. The color plots on the right identify gas and liquid regions.

can be seen in Fig. 12. The color contours in the figures represent two different quantities. In the right half of each panel, red identifies the gas/vapor region while blue identifies the water region. On the left half of each panel, the color contours identify the pressures in both the liquid and gas regions. These clearly show the development, as time evolves from Fig. 12(a) to (d), of very high pressure region resulting in the formation of the reentrant jet. The vector plots in each of the left frames shows the local instantaneous velocities and also clearly show the development of a high-speed region defining the reentrant jet, e.g. in Fig. 12(c) and (d).

Fig. 12 also shows a comparison of the bubble shapes (black lines for the experiment and white lines for the simulation) during bubble growth at $\bar{t} = 0.27$, depicted in Fig. 12(a). The comparison is very good at this instant and an almost spherical shape with a slightly flattened side near the wall is seen in both experiment and simulation. The other three comparisons are concerned with the bubble collapse phase at the normalized times, $\bar{t} = 1.9, \bar{t} = 2.09$, and$\bar{t} = 2.1$. These correspond to three times during the steep slope bubble collapse seen in Fig. 9. The bubble is seen to have taken an egg shape at $\bar{t} = 1.9$ (Fig. 12(b)) with a

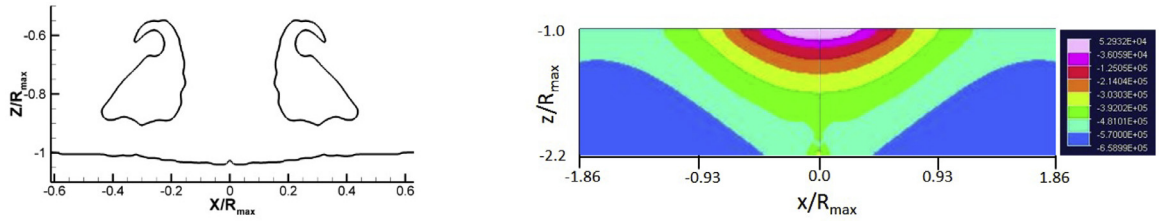

Fig. 13. (a) Shape of the Agar – water interface and toroidal bubble following reentrant jet impact at $\bar{t} = 2.245$. (b) Distribution of the stresses in the Agar layer. $\bar{X} = 1.05$.

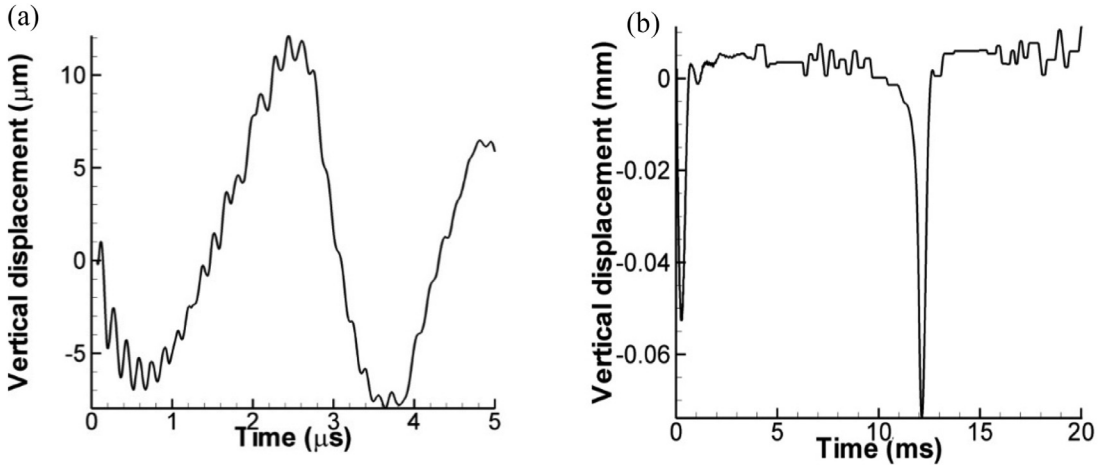

Fig. 14. Comparison of the vertical displacements of the interface center point for $\bar{X} = 1.0$ for Polyurea under (a) Cavitating jet erosive conditions and (b) Spark-generated bubbles under improper material scaling conditions. Cavitating jet conditions: $P_{amb} \sim 7$ MPa, $R_{max} = 0.1$ mm; thickness of Polyurea coating = 0.1 mm. Spark test conditions: $P_{amb} = 0.014$ MPa, $R_{max} = 20$ mm; thickness of Agar layer = 20 mm.

flattened side towards the wall at this earlier stage of the collapse. Comparing simulation to experiment, the match is good overall, with the top part of the bubble matching very well, while the lower part of the bubble facing the wall is seen to be over-flattened in the simulation. This so far unexplained trend continues during the reentrant jet development and penetration through the bubble. However, the shape and position of the reentrant jet at $\bar{t} = 2.09$ (Fig. 12(c)) as well as at $\bar{t} = 2.1$ (Fig. 12(d)) when the jet hits the bubble opposite wall, seem to be very well captured by the simulation.

Fig. 13 gives additional information from the numerical simulation. Fig. 13(a) taken at $\bar{t} = 2.245$ shows a zoom on the toroidal bubble shape following reentrant jet impact and the corresponding Agar interface deformation. Fig. 13(b) shows the corresponding stresses computed inside the Agar material.

5.3. Example of improper material scaling

It would be erroneous to use the same material and apply the scaling to only the bubble dynamics; i.e. use with the same coating a laboratory scale larger bubble to ease visualization to reproduce a smaller and fast collapsing bubble under the actual cavitation conditions. For instance, to examine the response of Polyurea to microscopic bubble collapse under high pressures, one cannot simply conduct spark-generated bubbles or laser generated bubbles at low pressure with Polyurea as the boundary material and deduce the response through Rayleigh scaling only.

To illustrate this, we compare in Fig. 14 the vertical displacement of a 0.1 mm thick Polyurea layer in response to two largely different bubble sizes. Fig. 14(b) shows the displacement due to a 20 mm maximum radius spark-generated bubble growing and collapsing in an ambient pressure of about 0.014 MPa. Fig. 14(a) shows the displacement due to a 0.1 mm maximum radius bubble growing and collapsing in an ambient pressure of about 7 MPa. As can be seen by comparing the two figures, the small bubble, which also has a very short period, generates a displacement of the Polyurea interface of an amplitude of about 10 μm, while the large relatively slow dynamics spark bubble, generates two large deformations following the initiation of the dynamics and at bubble collapse respectively and very small deformations in between. One could wrongly conclude from Fig. 14 that the spark conditions are more erosive.

However, if we follow through with the scaling reasoning, we should compare the results in normalized plots as shown in Fig. 15. As expected, the scaling of the bubble radius is very good between the two conditions. It is not perfect due to the terms neglected in the Rayleigh scaling such as the gas pressure inside the bubbles, surface tension, and compressibility effects.

On the other hand, trying to conclude about the material response based on the spark-test and the full scale material is a losing proposition. After normalizing properly, as in Fig. 15(b), the spark test material displacement has no connection with the cavitating jet conditions, both in terms of amplitude and qualitative shape of the curves. This highlights again the need to properly scale the material properties and not use the same material, as further demonstrated in the following section.

5.4. Examples of proper scaling: Polyurea vs. Agar 0.5%

In order to demonstrate a proper scaling, we follow the reasoning presented earlier using Tables 1 and 2. We recall from Table 2 that in order to simulate a cavitating jet tests at 7 MPa with a spark test at 0.014 MPa, we need for the spark tests a material whose deformation resistance parameters (G and E) are 7/0.014 = 500 times less than that of Polyurea. As discussed earlier (see Table 1), a 0.5% concentration Agar possesses such

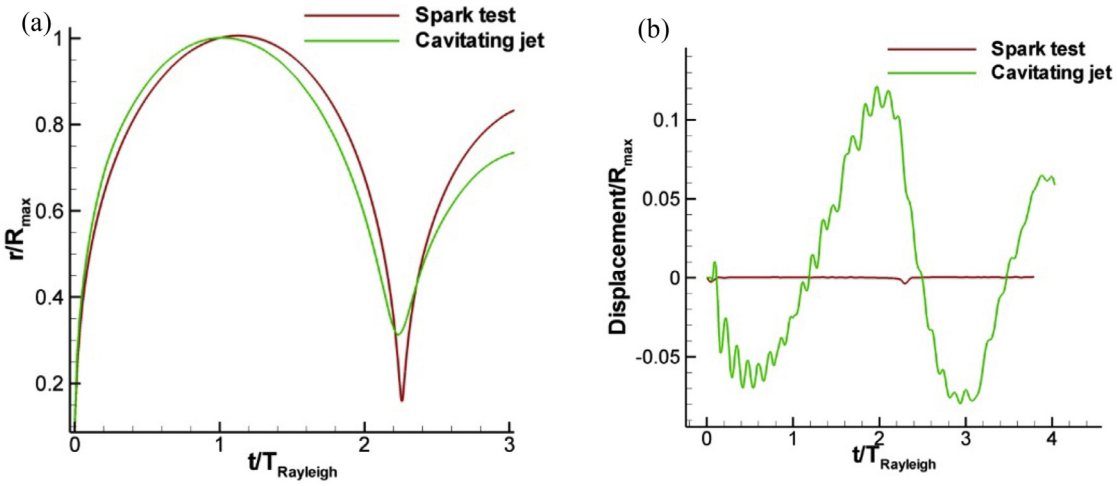

Fig. 15. Comparison of (a) the normalized bubble radii and (b) the normalized vertical displacements of the interface center point for the same simulation conditions as in Fig. 14.

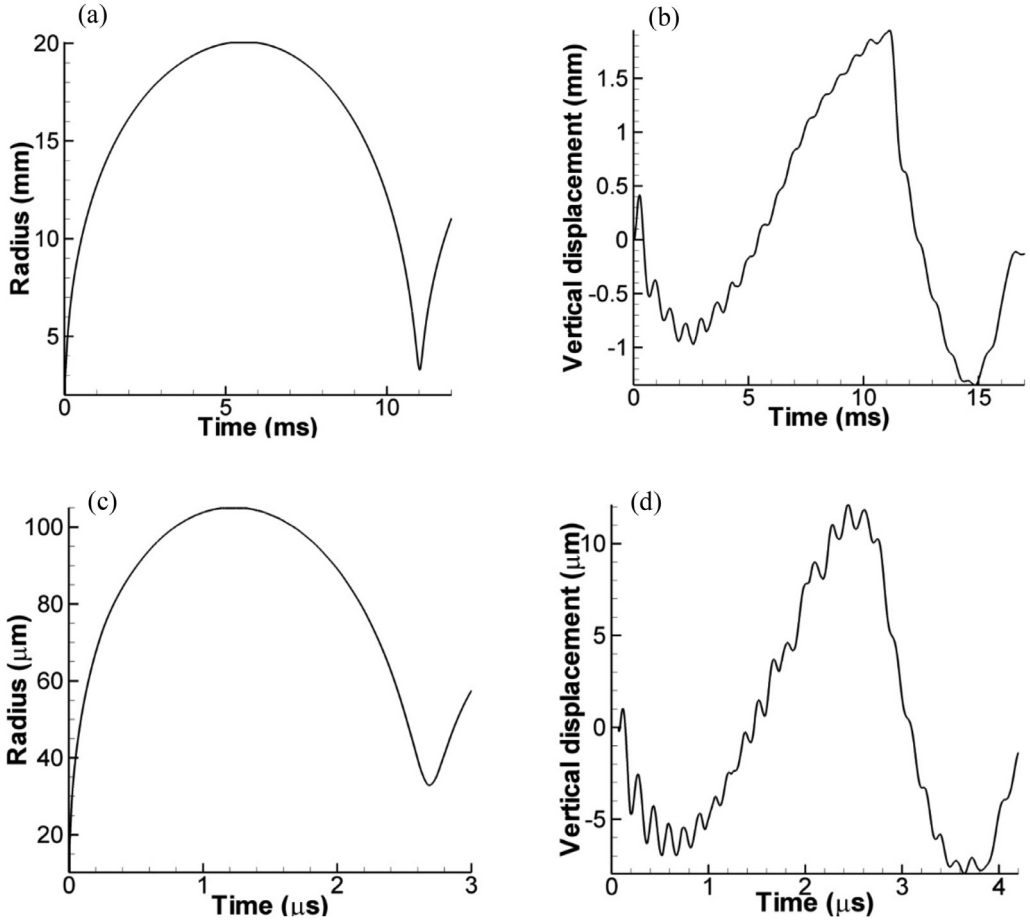

Fig. 16. Radius evolution and displacement of the interface center point for $\bar{X} = 1.5$ for (a), (b) spark-generated bubble conditions, $P_{amb} = 0.014$ MPa, $R_{max} \sim 20$ mm, 0.5% Agar and (c), (d) Bubble collapse in cavitating jet conditions, $P_{amb} \sim 7$ MPa, $R_{max} \sim 100$ μm, on Polyurea.

properties. Therefore, we conduct in this section FSI simulations with both Polyurea and 0.5% Agar under the respective conditions and examine the correspondence between the two results.

Results of the simulations in both dimensional and non-dimensional formats are shown in Fig. 16 through Fig. 19 for two non-dimensional standoff distances, $\bar{X} = 1.5$ and $\bar{X} = 1.0$, respectively. Fig. 16 shows the results of the simulation for $\bar{X} = 1.5$. Fig. 16(a) and (b) show the time evolution of the bubble equivalent radius and the displacement of the center point of the interface respectively for Agar 0.5%. Fig. 16(c) and (d) show the same for Polyurea. We can already see that the curves in the two sets have the same shapes and compare qualitatively very well. To compare more appropriately, the bubble equivalent radii are normalized with R_{max} and times with the Rayleigh time and compared together in Fig. 17(a). The two sets superpose quite well during most of the dynamics and differ by a small amount in the

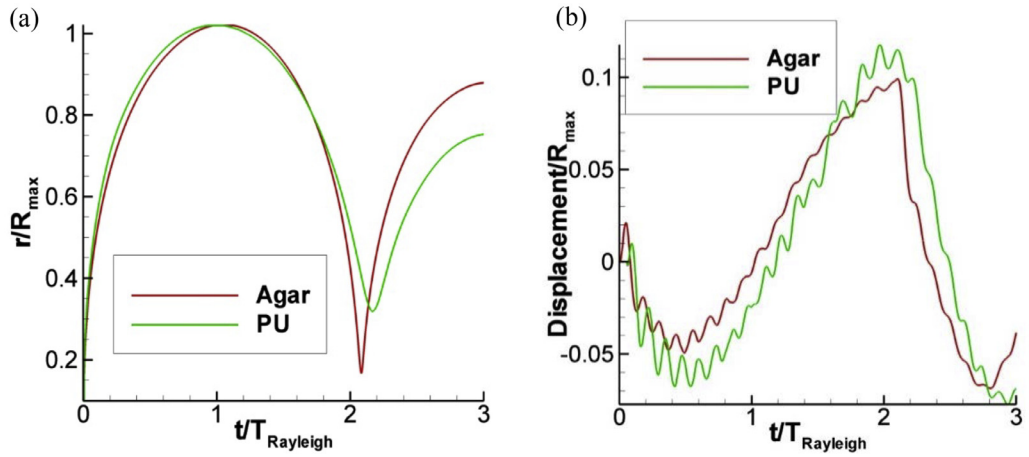

Fig. 17. Comparison of (a) the normalized bubble radii and b) the normalized vertical displacements of the interface center point for the same simulation conditions as in Fig. 16.

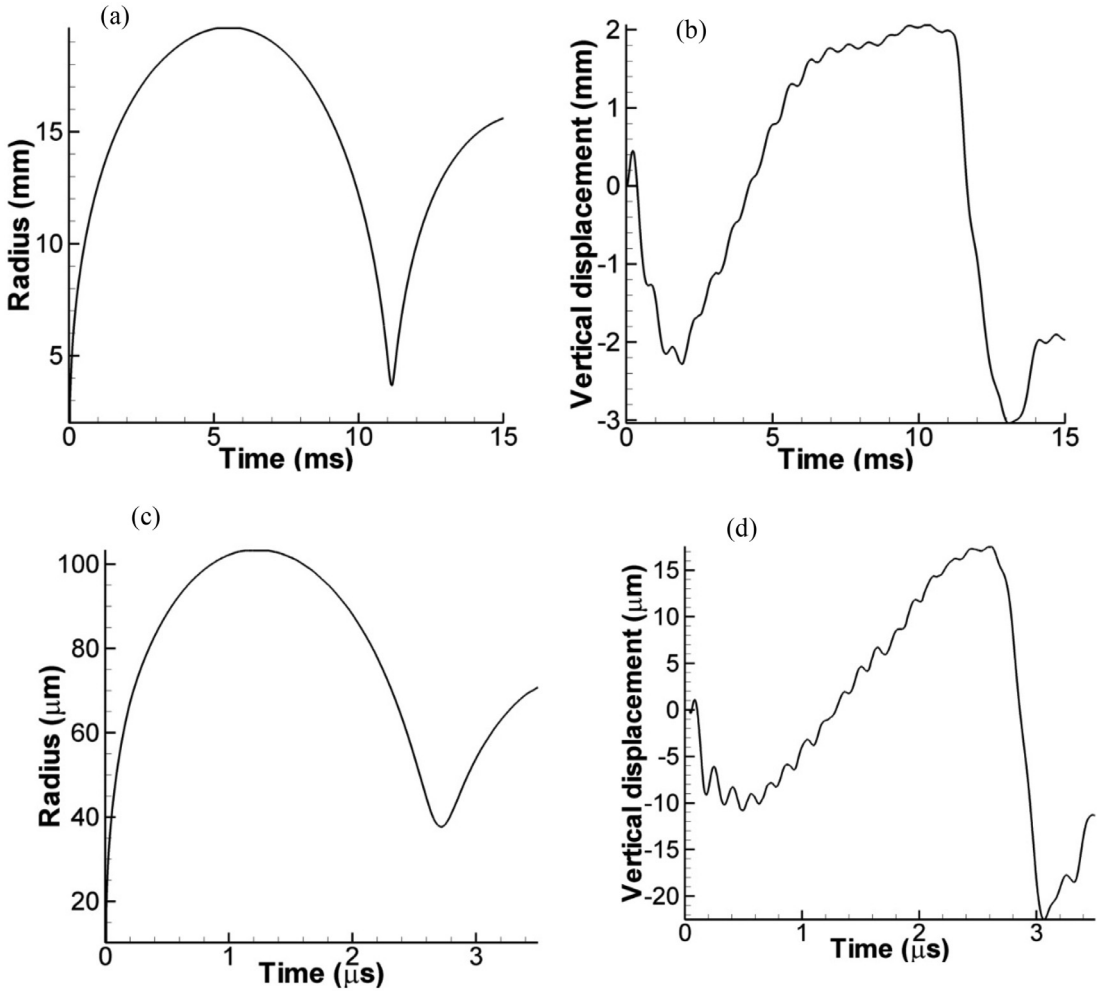

Fig. 18. Radius evolution and displacement of the interface center point for $\bar{X} = 1.0$ for (a), (b) spark-generated bubble conditions, $P_{amb} = 0.014$ MPa, R_{max}~20 mm, 0.5% Agar and (c), (d) Bubble collapse in cavitating jet conditions, P_{amb}~7 MPa, R_{max}~100 μm, on Polyurea.

later phase of the collapse. Here too, this discrepancy is due to the terms ignored in the Rayleigh scaling such as the gas pressure inside the bubbles, and compressibility effects, which are different between the two cases.

The material interfaces' displacement curves in Fig. 17(b), also show good correspondence indicating that the dominant physical effects occurring in the Polyurea response to a cavitation bubble collapse are captured very well with the 0.5% Agar both in terms of

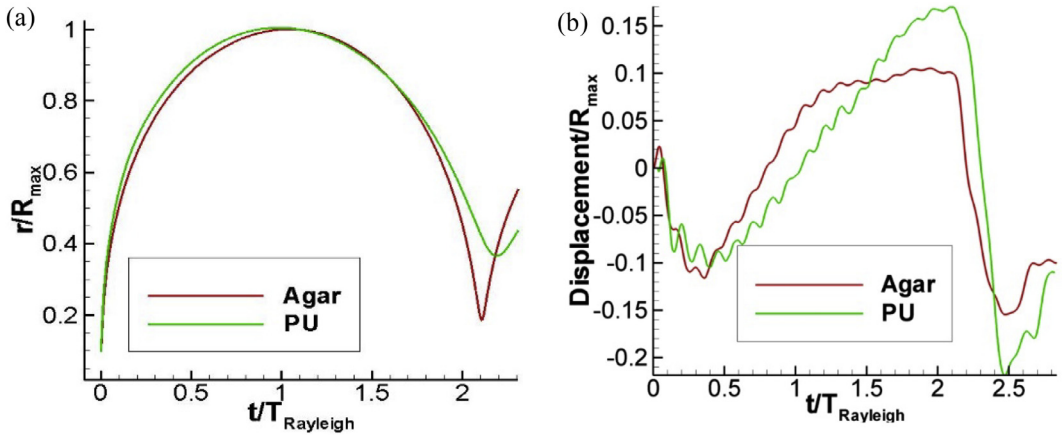

Fig. 19. Comparison of (a) the normalized bubble radii and (b) the normalized vertical displacements of the interface center point for the same simulation conditions as in Fig. 18.

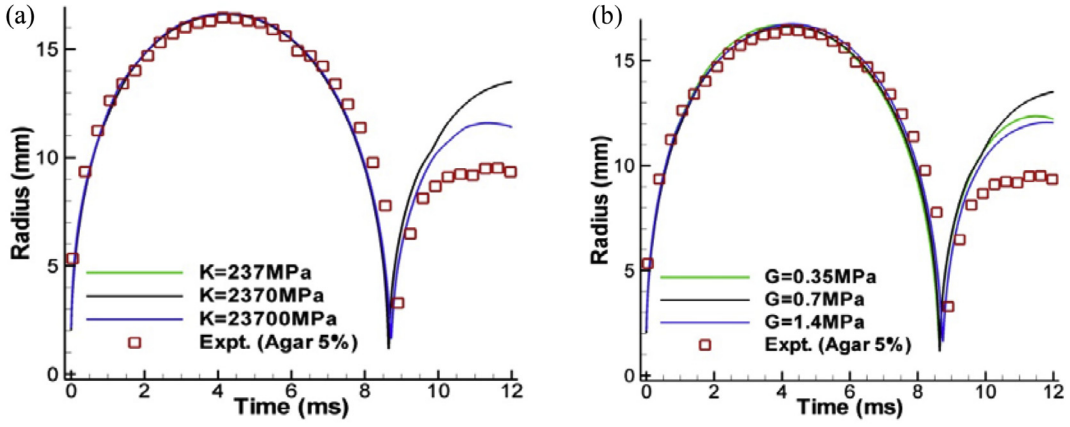

Fig. 20. Study of the effects of (a) the elastic bulk modulus, K and (b) the shear modulus G on the bubble equivalent radius time evolution for $\bar{X} = 1.5$ for Agar 5% under spark test conditions: thickness of Agar layer = 20 mm $P_{amb} = 0.014$ MPa, $R_{max} = 20$ mm. In (a) K = 237 MPa and K = 2,370 MPa curves are indistinguishable.

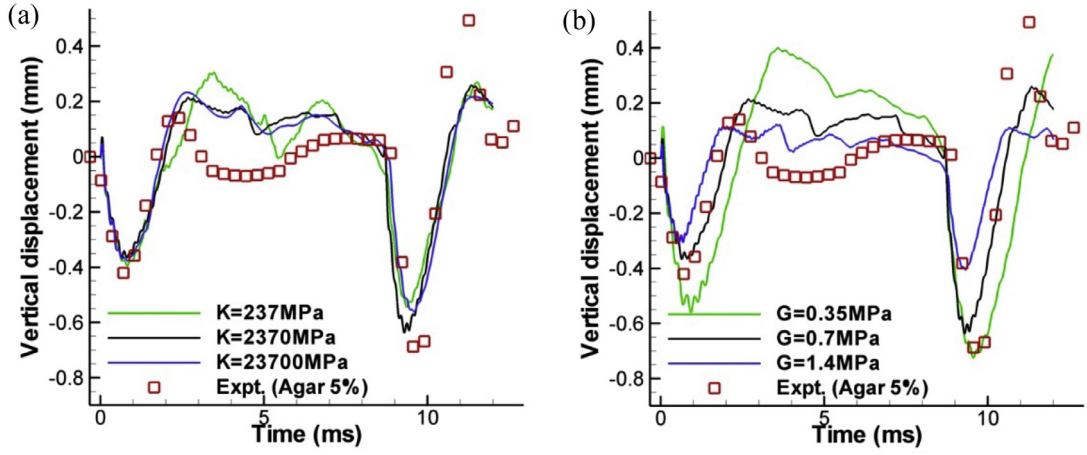

Fig. 21. Effects on the displacement of the center of the interface between Agar and water of: (a) the elastic bulk modulus, K and (b) the shear modulus G.$\bar{X} = 1.5$, thickness of 5% Agar layer = 20 mm, spark test conditions: $P_{amb} = 0.014$ MPa, $R_{max} = 20$ mm.

amplitude and timing. This shows that the procedure can be quite successful.

The same procedure is then repeated for a smaller bubble - coating standoff distance, $\bar{X} = 1.0$, and is shown in Figs. 18 and 19. Here again we see the same good correspondence between the two scaled configurations. The correspondence between the bubble radii up to the collapse time is very good, while in the later stages of the collapse, interface displacement shows some disagreement due to the physical parameters that are not scaled and also due to the imperfect knowledge of the materials properties. The ef-

fect of these properties on the results is examined in the next section.

5.5. Effects of the material properties

The material properties of Agar that were used in this study were obtained mainly from the literature (Chen et al., 2004, Nayar et al., 2012). However, there definitely are uncertainties in these selections and it is important to quantify the effects of these uncertainties. The viscoelastic model used in this study requires two elastic properties as input. Here, we specified the elastic bulk modulus and shear modulus, while the Young's modulus and Poisson's ratio were computed from the standard relations for elastic properties. In the following figures we examine the effects of these properties on the results, considering the cases in Fig. 7 where we compared simulations and spark tests.

Figs. 20 and 21 illustrate respectively the effect of changing the bulk modulus, K, by two orders of magnitude and the shear modulus, G, by a factor of 4. We believe that this exceeds by far any uncertainties. Since the cases considered here do not involve very strong effects of the material deformation on the bubble dynamics, the evolution of bubble radius versus time is very little affected by changing K and G, as illustrated in Fig. 20. K has practically no effect, while increasing G appears to have a very small discernable effect. The bubble period elongates by a negligible amount as the material becomes stiffer, which corroborates with our understanding that the bubble period is the longest for a rigid wall.

Discernable differences can, however, be observed in Fig. 21, which compares the displacement of the center of the interface while changing the material properties. Fig. 21(a) shows clearly that the bulk modulus, K, has practically no effect, since increasing K by two orders of magnitude just damped slightly the oscillations during the time where the bubble was at its maximum volume. However, these changes did not reduce the discrepancy with the spark tests near R_{max}. Fig. 21(b), on the other hand, shows a measurable effect of the shear modulus, G, (or also the Young's modulus, E, since they are connected) on the response of the Agar layer deformation. Increasing G (thus E) makes the material stiffer and reduces the amplitude of the unsteady material deformations. It also measurably reduces the material response time and reduces the time delay between the source of the excitation (initial pressure pulse and collapse pulse) and the corresponding maximum large deformation.

6. Conclusion

The study presented in this paper, shows that it is possible to properly simulate experimentally the fluid structure interaction problem of the interaction between a cavitation bubble and a coating layer using different but appropriately selected fluid and material conditions. For instance, a larger and slower evolving spark-generated bubble can be used to conduct visualizations and measurements to represent in a scaled fashion microscopic bubbles collapsing in a high jet pressure environment. To do this, the lengths are scaled using the bubble maximum equivalent radius, R_{max}, while times are scaled with the Rayleigh time. In addition, the materials' Young's moduli and shear moduli ratios have to be scaled by the maximum pressure generated at collapse of the bubble. To demonstrate this, spark-generated bubbles and numerical simulations involving fully coupled fluid structure interaction were used to demonstrate the scaling approach. The numerical FSI method was first validated against the spark-generated bubbles and was found to produce a very good agreement. The method was then used to demonstrate the validity of the scaling approach involving scaling both the liquid and bubble dynamics and the material dynamics. Micro meter size cavitating bubbles in a high ambient pressure on a layer of Polyurea coating were shown to have very good correspondence with centimetre size spark generated bubbles on an Agar layer in low ambient pressure. The factors that act as impediments to achieve perfect scaling were discussed and the effect of uncertainties in the material properties used in the simulations were investigated.

Acknowledgments

This work was supported by the Office of Naval Research under contract N00014-15-C-0052 monitored by Dr. Ki-Han Kim. We sincerely appreciate this support. We also are thankful to Mr. Gregory Harris, Naval Surface Warfare Center, Grant No. (N00174-15-D-0008) Indian Head Division, for providing us access to the Dysmas code.

References

Amirkhizi, A.V., Isaacs, J., McGee, J., Nemat-Nasser, S., 2006. An experimentally-based viscoelastic constitutive model for polyurea, including pressure and temperature effects. Philos. Mag. 86 (36), 5847–5866.
Borkent, B.M., Gekle, S., Prosperetti, A., Lohse, D., 2009. Nucleation threshold and deactivation mechanisms of nanoscopic cavitation nuclei. Phys. Fluids 21 (10), 102003.
Brennen, C.E., 1995. Cavitation and Bubble Dynamics. Cambridge University Press.
Brujan, E.A., Keen, G.S., Vogel, A., Blake, J.R., 2002. The final stage of the collapse of a cavitation bubble close to a rigid boundary. Phys. Fluids 14 (1), 85–92.
Chahine, G.L., 1982. Experimental and asymptotic study on nonspherical bubble collapse. Appl. Sci. Res. 38 (1), 187–197.
Chahine, G.L., 2004. Nuclei effects on cavitation inception and noise. In: Proceedings of the Twenty Fifth Symposium Naval Hydrodynamics.
Chahine, G.L., 2014. Modeling of cavitation dynamics and interaction with material. In: Kim, A., Chahine, K.-H., Franc, G.L., Karimi, J.-P. (Eds.), Advanced Experimental and Numerical Techniques for Cavitation Erosion Prediction. Springer, Berlin, pp. 123–173.
Chahine, G.L., Annasami, R., Hsiao, C.-T., Harris, G., 2002. Scaling of the *re*-entering jet parameters of an underwater explosion bubble below a floating structure. In: Proceedings of the Seventy Fourth Shock and Vibration Symposium.
Chahine, G.L., Franc, J.-P., Karimi, A., 2014. Laboratory testing methods of cavitation erosion. In: Kim, K.-H., Chahine, G.L., Franc, J.-P., Karimi, A. (Eds.). In: Advanced Experimental and Numerical Techniques, 160. Springer, Berlin, pp. 21–36.
Chahine, G.L., Frederick, G.S., Lambrecht, C.J., Harris, G.S., Mair, H.U., 1995. Spark generated bubbles as laboratory-scale models of underwater explosions and their use for validation of simulation tools. In: *Proceedings of the Sixty Sixth Shock and Vibration Symposium*, 2, pp. 265–276.
Chahine, G.L., Hsiao, C.-T., 2015. Modeling cavitation erosion via bubble–material interaction. Interface Focus 5 (5), 20150016.
Chahine, G.L., Kalumuck, K.M., 1997. The influence of structural deformation of water jet impact loading. J. Fluids Struct. 12 (1), 103–121. doi:10.1006/jfls.1997.0127.
Chahine, G.L., Kapahi, A., Choi, J.-K., Hsiao, C.-T., 2015. Modeling of surface cleaning by cavitation bubble dynamics and collapse. Ultrason. Sonochem. 29, 528–549.
Chen, Q., Suki, B., An, K.-N., 2004. Dynamic mechanical properties of Agarose gel by a fractional derivative model. J. Biomech. Eng. 126 (5), 666–671.
Choi, J.-K., Chahine, G.L., 2017. Experimental and numerical study of polyurea failure under cavitation. In: Proceedings of the Fifth International Symposium on Marine Propulsors.
Choi, J.K., Chahine, G.L., 2003. Non-spherical bubble behavior in vortex flow fields. Comput. Mech. 32 (4–6), 281–290.
Cole, R.H., 1965. Underwater Explosions. Dover Publications.
Crum, L., 1979. Surface oscillations and jet development in pulsating bubbles. J. Phys. Colloq. 40 (C8), C8–85.
Duncan, J.H., Zhang, S., 1991. On the interaction of a collapsing cavity and a compliant wall. J. Fluid Mech. 226, 401–423.
Ellis, A.T., 1965. Parameters Affecting Cavitation and Some New Methods For Their Study. California Institute of Technology Technical Report, October.
Fuster, D., Colonius, T., 2011. Modelling bubble clusters in compressible liquids. J. Fluid Mech. 688, 352–389.
Gnanaskandan, A., Mahesh, K., 2015. A numerical method to simulate turbulent cavitating flows. Int. J. Multiph. Flow 70, 22–34.
Goh, B.H.T., Gong, S.W., Ohl, S.-W., Khoo, B.C., 2017. Spark-generated bubble near an elastic sphere. Int. J. Multiph. Flow 90, 156–166.
Hamaguchi, F., Ando, K., 2015. Linear oscillation of gas bubbles in a viscoelastic material under ultrasound irradiation. Phys. Fluids 27 (113103). doi:10.1063/1.4935875.
Hammitt, F.G., 1980. Cavitation and Multiphases Flow Phenomena. McGraw-Hill.
Hsiao, C.-T., Chahine, G.L., 2015. Dynamic response of a composite propeller blade subjected to shock and bubble pressure loading. J. Fluids Struct. 54, 760–783.
Hsiao, C.-T., Jayaprakash, A., Kapahi, A., Choi, J.-K., 2014. Modeling of material pitting from cavitation bubble collapse. J. Fluid Mech. 755, 142–175.

Jamburidze, A., De Corato, M., Huerre, A., Pommella, A., Garbin, V., 2017. High-frequency linear rheology of hydrogels probed by ultrasound-driven microbubble dynamics. Soft Matter 13 (21), 3946–3953.
Jayaprakash, A., Chahine, G.L., Hsiao, C.-T., 2012. Numerical and experimental study of the interaction of a spark-generated bubble and a vertical wall. ASME J. Fluids Eng. 134 (3), 31301–31312.
Kapahi, A., Hsiao, C., Chahine, G., 2015. A multi-material flow solver for high speed compressible flows. Comput. Fluids 115, 25–45.
Key, S.W., 1974. A finite element procedure for the large deformation dynamic response of axisymmetric solids. Comput. Methods in Appl. Mech. Eng. 4 (2), 195–218.
Kim, K.-H., Chahine, G., Franc, J.-P., Karimi, A. (Eds.). Advanced Experimental and Numerical Techniques For Cavitation Erosion Prediction, (Vol. 106), 2014. Springer, Netherlands.
Kinnas, S., Fine, N., 1994. A nonlinear boundary element method for the analysis of unsteady propeller sheet cavitation. In: Proceedings of the Ninteenth Symposium on Naval Hydrodynamics.
Kinzel, M.P., Lindau, J.W., Kunz, R.F., 2009. A level-set approach forlLarge scale cavitation. In: Proceedings of the DoD High Performance Computing Modernization Program Users Group Conference.
Kling, C., 1970. A high speed photographic study of cavitation bubble collapse Ph.D. Thesis. University of Michigan.
Kling, C.L., Hammitt, F.G., 1972. A Photographic study of spark-induced cavitation bubble collapse. J. Basic Eng. 94 (4), 825–832.
Krieger, J.R., Chahine, G.L., 2003. Dynamics and acoustic signature of non-spherical underwater explosion bubbles. In: Proceedings of the Seventy Fourth Shock and Vibration Symposium.
Kulik, V.M., 2007. Forced oscillations of a layer of a viscoelastic material under the action of a convective pressure wave. J. Appl. Mech. Tech. Phys. 48 (2), 221–228.
Lauterborn, W., Bolle, H., 1975. Experimental investigations of cavitation-bubble collapse in the neighbourhood of a solid boundary. J. Fluid Mech. 72, 391–399.
Lauterborn, W., Lechner, C., Mettin, M., Robert, K., 2018. Bubble models and real bubbles: Rayleigh and energy-deposit cases in a Tait-compressible liquid. IMA J. Appl. Math. 83 (4), 556–589.
Rayleigh, L., 1917. On the pressure developed in a liquid during the collapse of a spherical cavity. Philos. Mag. Ser. 6 34 (200), 94–98.
Luton, J.A., Wardlaw, A., Chahine, G.L., Hsiao, C.-T., 2004. Simulation of surface vessel hull whipping response using fully-coupled hydrocodes. In: *Proceedings of the Seventy Fifth Shock and Vibration Symp*osium.
Ma, J., Hsiao, C.-T., Chahine, G.L., 2015. Euler–Lagrange simulations of bubble cloud dynamics near a wall. J. Fluids Eng. 137 (4), 041301.
Ma, J., Hsiao, C.-T., Chahine, G.L., 2018a. Numerical study of bubble cloud dynamics near a rigid wall. Ultrason. Sonochem. 40, 944–954.
Ma, X., Huang, B., Zhao, X., Wang, Y., Chang, Q., et al., 2018b. Comparisons of spark-charge bubble dynamics near the elastic and rigid boundaries. Ultrason. Sonochem. 43, 80–90.
Madadi-Kandjani, E., Xiong, Q., 2014. Validity of the spring-backed membrane model for bubble-wall interactions with compliant walls. Comput. Fluids 96, 116–121.
Marlin, P., Chahine, G.L., 2018. Erosion and heating of Polyurea under cavitating jets. Wear 414, 262–274.
Movahed, P., Kreider, W., Maxwell, A.D., Hutchens, S.B., Freund, J.B., 2016. Cavitation-induced damage of soft materials by focused ultrasound bursts: a fracture-based bubble dynamics model. J. Acoust. Soc. Am. 140 (2), 1374–1386.
Naudé, C.F., Ellis, A.T., 1961. On the mechanism of cavitation damage by nonhemispherical cavities collapsing in contact with a solid boundary. J. Basic Eng. 83 (4), 648–656.
Nayar, V.T., Weiland, J.D., Nelson, C.S., Hodge, A.M., 2012. Elastic and viscoelastic characterization of agar. J. Mech. Behav. Biomed. Mater. 7, 60–68.
Plesset, M.S., 1964. Bubble dynamics and cavitation in real liquids. In: Davies, R. (Ed.), Proceedings of the Symposium on cavitation in real liquids. General Motors Research Laboratories, Warren, Michigan, pp. 1–17.
Plesset, M.S., Chapman, R.B., 1971. Collapse of an initially spherical vapour cavity in the neighbourhood of a solid boundary. J. Fluid Mech. 47 (2), 283–290.
Singhal, N.H., Athavale, A.K., Li, M., Jiang, Y., 2002. Mathematical basis and validation of the full cavitation model. J. Fluids Eng. 124 (3), 618–624.
Snay, H.G., Christian, E.A., 1952. Underwater explosion phenomena: the parameters of non-migrating bubble oscillating in an incompressible medium. US Navy *Navord Report*. 2437.
Vogel, A., Lauterborn, W., Timm, R., 1989. Optical and acoustic investigations of the dynamics of laser-produced cavitation bubbles near a solid boundary. J. Fluid Mech. 206, 299–338.
Wang, C., Khoo, B.C., 2004. An indirect boundary element method for three-dimensional explosion bubbles. J. Comput. Phys. 194 (2), 451–480.
Wardlaw, A., Luton, J.A., 2003. The Gemini Euler solver for the coupled simulation of underwater explosions. US Navy *NSWCIH - Technical Report* (2500).
Whirley R.G.G., Engelmann B.E.E. 1993. DYNA3D: A nonlinear, explicit, three dimensional finite element code for solid and structural mechanics - user manual. Livermore, CA.
Zel'dovich, Y.B., Raizer, Y.P., 2012. Physics of Shock Waves and High-Temperature Hydrodynamic Phenomena. Courier Corporation.
Zhang, S., Duncan, J., Chahine, G.L., 1993. The final stage of the collapse of a cavitation bubble near a rigid wall. J. Fluid Mech. 257, 147–181.